



The Ultraviolet Visible Hyperspectral Imaging Spectrometer (UVHIS), and high-resolution NO₂ mapping from its first airborne observation

Liang Xi ^{1,2}, Fuqi Si ¹, Yu Jiang ¹, Haijin Zhou ¹, Kai Zhan ¹, Zhen Chang ¹, Xiaohan Qiu ¹ and
5 Dongshang Yang ^{1,2}

¹Key Laboratory of Environmental Optics and Technology, Anhui Institute of Optics and Fine Mechanics, Chinese Academy of Sciences, Hefei 230031, China

² University of Science and Technology of China, Hefei, 230026, Anhui, China

Correspondence to: Fuqi Si (sifuqi@aiofm.ac.cn)

10 **Abstract.** We present a novel airborne imaging differential optical absorption spectroscopy (DOAS) instrument: Ultraviolet
Visible Hyperspectral Imaging Spectrometer (UVHIS), which is developed for trace gas monitoring and pollution mapping.
Within a broad spectral range from 200 to 500 nm, operated in three channels, the spectral resolution of UVHIS is better
than 0.5 nm. The optical design of each channel comprises a fore-optics with a field of view (FOV) of 40°, an Offner
imaging spectrometer, and a charge-coupled device (CCD) array detector of 1032 × 1072 pixels. A first demonstration flight
15 using UVHIS was undertaken on 23 June 2018, above an approximate 600 km² area in Feicheng, China, with a spatial
resolution of about 25 × 22 m². Measurements of nadir backscattered solar radiation of channel 3 are used to retrieve vertical
column densities (VCDs) of NO₂ with a mean fitting error of 2.6 × 10¹⁵ molec cm⁻². The UVHIS instrument clearly detected
several emission plumes transporting from south to north, with a peak value of 3 × 10¹⁶ molec cm⁻² in the dominant one.
UVHIS NO₂ vertical columns are well correlated with ground-based mobile DOAS observations, with a correlation
20 coefficient of 0.65 for all co-located measurements, and a slight underestimation for polluted observations. This study
demonstrates the capability of UVHIS for NO₂ local emission and transmission monitoring.

1 Introduction

Nitrogen oxides (NO_x), the sum of nitrogen monoxide (NO) and nitrogen dioxide (NO₂), plays a key role in the chemistry of
the atmosphere, such as the ozone destruction in the stratosphere (Solomon, 1999), and the secondary aerosol formation in
25 the troposphere (Seinfeld and Pandis, 2016). In the troposphere, despite lightning, soil emissions and other natural processes,
the main sources of NO_x are anthropogenic activities like fossil fuel combustion by power plants, factories, and road
transportation, especially in the urban and polluted regions. As an indicator of anthropogenic pollution, the amounts and
spatial distributions of NO_x attract large attention.

Compared to NO, Nitrogen dioxide (NO₂) is more stable in the atmosphere. Based on the characteristic absorption structures
30 of NO₂ in the ultraviolet-visible spectral range, the differential optical absorption spectroscopy (DOAS) technique has been



well applied to retrieve the light path integrated densities from different platforms (Platt and Stutz, 2008). Combining the imaging spectroscopy technique, imaging DOAS instruments were developed in recent years to determine the trace gases temporal variation as well as the two dimensional distribution. Global horizontal distribution of tropospheric NO₂ and other trace gases has been mapped and studied by several space-borne sensors, including SCIAMACHY (Scanning Imaging Absorption Spectrometer for Atmospheric CHartography; Bovensmann et al., 1999), GOME (Global Ozone Monitoring Experiment; Burrows et al., 1999) and GOME-2 (Munro et al., 2016), OMI (Ozone Monitoring Instrument; Levelt et al., 2006) and TROPOMI (TROPospheric Ozone Monitoring Instrument; Veefkind et al., 2012). The Environmental trace gases Monitoring Instrument (EMI; Cheng et al., 2019; Zhao et al., 2018), as the first designed space-borne sensor in China, was launched on 9 May 2018, on-board the Chinese GaoFen-5 (GF5) satellite. In terms of spatial resolution, the majority of these space-borne sensors are lower than $10 \times 10 \text{ km}^2$, except TROPOMI with a relative higher resolution of $3.5 \times 5.5 \text{ km}^2$.

In order to achieve spatial resolution higher than $100 \times 100 \text{ m}^2$ for investigation of spatial distribution in urban areas and individual source emissions, several researches have applied the imaging DOAS instruments on airborne platforms. The airborne imaging DOAS measurement was firstly performed by Heue et al. (2008) over South African Highveld plateau. For the purpose of retrieval of urban NO₂ horizontal distribution, Popp et al. (2012) and Lawrence et al. (2015) performed their measurements separately in Zürich, Switzerland, and Leicester, England. In 2013, an airborne measurement focusing on source emissions was performed in China, over Tianjin, Tangshan and Bohai gulf (Liu et al., 2015). An inter-comparison study of four airborne imaging DOAS instruments over Berlin, Germany, suggests a good agreement between different sensors, and the effectiveness of imaging DOAS to reveal the fine-scale horizontal variability in tropospheric NO₂ in an urban context (Tack et al., 2019).

Here we present a novel airborne imaging DOAS instrument: Ultraviolet Visible Hyperspectral Imaging Spectrometer (UVHIS), designed and developed by Anhui Institute of Optics and Fine Mechanics, Chinese Academy of Sciences (AIOFM, CAS). As a hyperspectral imaging sensor with high spectral and spatial resolution, UVHIS is designed to be operated on aircraft platform for the purpose of atmospheric trace gas measurements and pollution monitoring over large area in a relative short time frame. By using the DOAS technique and geo-referencing, two dimensional spatial distribution of its first demonstration flight over Feicheng, China is also presented in this paper.

The organization of this paper is listed as follows: Sect. 2 presents a technical description of UVHIS system, as well as its preflight calibration results. Section 3 introduces the detailed information of its first research flight above Feicheng, China. Section 4 describes the developed algorithm for retrieval and geographical mapping of NO₂ vertical column densities from hyperspectral data. Section 5 present the retrieved NO₂ column densities, and Section 6 compares airborne measurements with correlative ground-based data sets from a mobile DOAS system.



2 Instrument Details

1.1 The UVHIS instrument

UVHIS is a hyperspectral instrument measuring nadir backscattered solar radiation in the ultraviolet and visible wavelength region from 200 to 500 nm. The instrument is operated in three channels at wavelength 200-276 nm (channel 1), 276-380 nm
65 (channel 2) and 380-500 nm (channel 3) for minimal stray light effects and highest spectral performance. The main characteristics of UVHIS are summarized in Table 1.

As shown in Fig. 1, the optical benches of three channels share a similar design, consisting of a telecentric fore-optics, an Offner imaging spectrometer, and a two dimensional charge-coupled device (CCD) array detector. The Offner imaging spectrometer consists of a concave mirror and a convex grating. Backscattered light below the aircraft is collected by a wide-
70 field telescope with a FOV of 40° in the across-track dimension. After passing through a bandpass filter and a 12.5 mm long entrance slit in the focal plane, light is reflected and diffracted by a concave mirror and a convex grating. The dispersed light is imaged onto a frame transfer CCD detector, which consists of 1032 × 1072 individual pixels. For the purpose of alignment and slight adjustment of the spectrometer, only the central 1000 rows of pixel are well illuminated in the across-track dimension. In the wavelength dimension, the image covers central 1024 columns of pixels on the CCD detector while the left
75 and right edge are used to monitor dark current. The spectral sampling and spectral resolution of all three channels can be found in Table 1.

To reduce dark current and improve signal-to-noise ratio (SNR) of the instrument, CCD detector is thermally stabilized at -20°C with a temperature stability of ± 0.05°C (Zhang et al., 2017). However, the optical bench is not thermally controlled, because all the instrument is mounted inside the aircraft platform which is basically temperature consistent. UVHIS is
80 mounted on a Leica PAV-80 gyro-stabilized platform that provides angular motion compensation. A high-grade Applanix navigation system on-board is used to receive the position (i.e. latitude, longitude, and elevation) and orientation (i.e. pitch, roll, and heading) information, which is required for accurate geo-referencing. The UVHIS instrument telescope collect solar radiation backscattered from the surface and atmosphere through a fused silica window on the bottom of the aircraft. In the case of NO₂ measurement, all observations in this study only use the channel 3.

85 2.2 Preflight calibration

In order to reduce errors in spectral analysis, spectral and radiometric calibration in the laboratory before actual airborne observation is very necessary.

For radiometric calibration, we use an integrating sphere with a tungsten halogen lamp for channel 2 and channel 3. While for channel 1, a diffuser plate with a Newport xenon lamp is used for a sufficient ultraviolet output. With the help of a well
90 calibrated spectral radiometer to monitor the radiance of calibration system, digital numbers (DNs) from CCD detectors of three channels can be converted to radiance correctly. Uncertainty of absolute radiance calibration of UVHIS is 4.89 % for channel 1, 4.67 % for channel 2 and 4.42 % for channel 3.



95 The preflight wavelength calibration was also performed in the laboratory, using a mercury–argon lamp and a tunable laser as sources. We model the slit function of UVHIS using a symmetric Gaussian function. Spectral registration and slit function calibration are achieved by least square fitting of characteristic lines in collected spectra. Table 2 lists the retrieved full-width at half maximums (FWHMs) for channel 3.

3 Research flight

100 The first demonstration flight above Feicheng city, Shiheng town and neighbouring rural areas was performed on 23 June 2018, aiming at producing NO₂ field maps of large area in a relative short time frame. UVHIS was operated from the Y-5 aircraft at altitude of 3 km above sea level, higher than the height of planetary boundary layer (PBL), with an average aircraft ground speed of 50 m/s. An overview of the observation area and flight lines is provided in Fig. 2. The aircraft took off at local noon from the airfield in Pingyin county, about 19 km northwest of the centre of the field. An area of approximately 600 km² was covered in 3 h, under clean sunny and cloudless conditions with low-speed southerly winds.

105 Research flight consists of 13 parallel lines in the east-west direction, starting from the lower left corner in Fig. 2. The distance between adjacent lines is 1.5 km, while the swath width of each individual line is about 2.2 km. Gapless coverage between adjacent lines can be guaranteed in this pattern because of the adequate overlap. To validate the NO₂ column densities retrieved from UVHIS by comparison to ground measurements, mobile DOAS measurements were performed inside the research area on the same day. As shown in Fig. 5, the measurements of the mobile DOAS system basically circle around the steel factory and the power plant, which are the presumed major emission sources inside the observation area.

110 At a typical flight altitude of 3 km in the Feicheng demonstration flight, the 40° FOV results in a swath width of 2.2 km on the ground. In the condition of spatial binning by 10 pixels across-track, the spatial resolution of the ground pixel in this direction is about 22 m. Meanwhile along-track spatial resolution is determined by the product of the detector integration time and the aircraft ground speed, with some variation due to aircraft pitch angle. At typical aircraft ground speed of 50 m/s and integration time of 0.5 s, the along-track spatial resolution of the ground pixel is about 25 m.

115 4 Data processing chain

NO₂ vertical column density (VCD) retrieval algorithm of UVHIS consists of four major steps. First, some necessary preprocessing procedures are required before any spectral analysis of UVHIS data. Next, UVHIS spectral data after preprocessing are analyzed in a suitable wavelength region by application of the well-established DOAS technique. After that, air mass factors (AMFs) are calculated for every observation based on SCIATRAN radiative transfer model to convert 120 the slant column densities (SCDs) to vertical column densities. In the final step, combining with sensor position and orientation information, NO₂ VCDs are geo-referenced and overlaid onto Google satellite map layers.



4.1 Preprocessing

The preprocessing procedure before spectral analysis includes data selection, dark current correction, spatial binning, and in-flight calibration. First, the spectral data acquired during U-turns of aircraft are removed in the processing because of the large and changing orientation angles. Also a threshold of radiance values is set to neglect some over-illuminated ground pixels inside the flight area, which are usually caused by presence of cloud or water mirror reflection.

The dark current correction is performed based on the measurement at the start of the entire flight by blocking the fore-optics, which is necessary to improve instrument performance and reduce analysis error in DOAS fit.

In order to increase the SNR of the instrument and the sensitivity to NO₂, the raw pixels of imaging DOAS are usually aggregated in across-track direction and across-track direction. According to photon statistics when only shot noise is considered, the SNR should rise with square root of number of binned spectra. However, this improved SNR of instrument results a reduction of spatial resolution. In data analysis of Feicheng flight, we use binning of 10 pixels in across-track direction, resulting in a ground pixel size of about 25 × 22 m².

Since the wavelength-to-pixel registration and the slit function shape of UVHIS could change compared to laboratory calibration results, in-flight wavelength calibration is essential for the next DOAS analysis. This in-flight wavelength calibration is achieved by fitting the measured spectra to a high-resolution solar reference (Chance and Kurucz, 2010) with slit function convolution and wavelength shift. The nominal wavelength-to-pixel registration determined in laboratory calibration, is used as initial values in the iteratively fitting procedure for convergence to the optimal solution. The effective shifts and FWHMs of different across-track position are plotted in Fig. 3. Results at three wavelengths are shown: blue for 430 nm (the start of the analysis wavelength region), green for 450 nm (the middle of the analysis wavelength region) and red for 470 nm (the end of the analysis wavelength region).

4.2 DOAS analysis

After preprocessing, the observed UVHIS spectra are analysed by the application of QDOAS (Danckaert et al., 2020) software in order to retrieve NO₂ slant column densities. The basic idea of the DOAS approach is to separate broadband signals like surface reflectance and Rayleigh scattering, and narrow-band signals like trace gas molecular absorption. The fitting window is within 430 and 470 nm wavelength region, considered to contain strongly structured NO₂ absorption features, and with low interference of other trace gases such as O₃, O₄. Absorption cross-sections of NO₂ and other trace gases and a synthetic Ring spectrum are simultaneously fitted to the logarithm of the ratio of the observed spectrum and a reference spectrum. These cross sections are made by convolving the high-resolution cross sections with in-flight wavelength calibration results for all across-track positions. Further details of the DOAS analysis setting can be found in Table 3.

For each analysed spectrum, the direct result of the DOAS fit is differential slant column density (dSCD), which is the difference of NO₂ integrated concentration along the effective light path between the studied spectrum and the selected



reference spectrum (SCD_{ref}). Reference spectra is acquired over a clean rural area upwind of the urban and factory areas, in
155 the lower left corner of Fig. 2. In the quite homogeneous background area, several spectra were averaged to increase the
SNR of the reference spectrum. For the purpose of avoiding across-track biases, a reference spectrum is required for each
across-track detector because of its intrinsic spectral response. Under the assumption that the spatial and temporal variability
of the stratospheric NO_2 field is negligible during the test flight, this approach eliminates the stratospheric NO_2 contribution,
making the results only sensitive to the tropospheric portion. According to Popp et al. (2012), the residual NO_2 amount in the
160 background spectrum is estimated to be 1×10^{15} molec cm^{-2} .

A sample NO_2 DOAS fit result and corresponding residual of UVHIS spectra is illustrated in Fig. 4, with a differential slant
column density (dSCD) of $5.05 \pm 0.38 \times 10^{16}$ molec cm^{-2} and a RMS on the residuals of 4.56×10^{-3} . The direct output of the
applied DOAS fitting algorithm are dSCDs.

4.3 Air mass factor calculations

165 SCD is the integrated concentration along the effective light path of observation, which is strongly dependent on the viewing
geometry and the radiative transfer. VCD is the integrated concentration along a single vertical transect from the Earth's
surface to the top of the atmosphere, which is independent of changes in the light path length of SCD.

$$VCD_i = \frac{dSCD_i + SCD_{ref}}{AMF_i} = \frac{dSCD_i + VCD_{ref} \times AMF_{ref}}{AMF_i} \quad (1)$$

As shown in Eq. (1), dSCDi from the DOAS fit can be converted to VCDi by dividing the AMFi which accounts for
170 enhancements in the light path (Solomon et al., 1987). In this study, NO_2 AMFs have been computed using the SCIATRAN
(Rozanov et al., 2014) radiative transfer model (RTM). SCIATRAN model numerically calculates AMFs based on a priori
information on the parameters that change effective light path, such as sun and viewing geometry, trace gas and aerosol
vertical profiles, surface reflectance etc.

4.3.1 Parameters in RTM

175 (1) During the flight, viewing geometry is retrieved from the orientation information of the aircraft. Solar position defined by
the solar zenith angle (SZA) and solar azimuth angle (SAA), as well as relative azimuth angle (RAA) can be calculated,
based on the time information, latitude and longitude position of each observation. (2) Since the flight is performed under
clear-sky condition, the effect of cloud presence can be neglected in AMF computation. (3) Surface reflectance used in AMF
calculation is the product of the Landsat 8 Operational Land Imager (OLI) space-borne instrument (Barsi et al., 2014).
180 Coastal aerosol band (433 to 450 nm) is selected because its bandwidth is relatively narrow, and this band is basically inside
the DOAS fitting window (Vermeote et al., 2016). (4) Since no accurate trace gas vertical profile is available during the flight,
a well-mixed vertical distribution (box profile) of NO_2 in the PBL is assumed. However, accurate PBL height is also
unavailable, a typical height of 2 km is a reasonable guess in the case of sunny summer day in mid-latitude area in China. (5)
Aerosol optical Depth (AOD) information used in AMF calculation is MODIS AOD product at 470 nm (Remer et al., 2005),



185 because neither ground-based aerosol measurement is performed, nor any AERONET station data near the flight area is available. Like the NO₂ profile, the aerosol extinction box profile is constructed from the PBL height and AOD. Single scattering albedo (SSA) is assumed to be 0.93, and asymmetry factor is assumed to be 0.68 for aerosol extinction profile.

The radiative transfer equation in SCIATRAN is solved in a pseudo-spherical multiple scattering atmosphere, using the scalar discrete ordinate technique. Simulations are performed for sensor altitude of 3 km above sea level, and wavelength of
190 the middle of the NO₂ fitting windows, i.e. 450nm. A NO₂ AMF look-up table (LUT) was computed, with different RTM parameter settings provided in Table 4. For each retrieved dSCD, an AMF was linear interpolated from the LUT based on the sun geometry, viewing geometry, and surface reflectance.

4.3.2 RTM dependence study

1. AMF dependence on the surface reflectance

195 As shown in Fig. 5, a time series of computed AMFs is plotted for research flight on 23 June 2018, as well as the corresponding surface reflectance, solar zenith angles, and relative azimuth angles. Other RTM parameters used in the AMF calculations are also provided in Fig. 5. Note that only data of nadir observations are plotted for a clearer display, and time gaps between adjacent flight lines can be observed. Despite the greater degree of varieties in viewing and sun geometries, it is obvious that the AMFs strongly depend on the surface reflectance. Previous studies reported in Lawrence et al. (2015),
200 Meier et al. (2017) and Tack et al. (2017) suggest a similar conclusion. A sensitivity test was carried out to investigate the impact of surface reflectance on the AMF calculations, based on SCIATRAN model with varying value of surface reflectance, and fixed value of other parameters. Results of this test is shown in Fig. 6, indicate that the relation between surface reflectance and AMF is non-linear. Especially when surface reflectance is blow 0.1, AMF increase with surface reflectance rapidly.

205 Generally speaking, the AMF should be higher in the case of a bright surface reflectance, because more sunlight is reflected from the ground back to atmosphere and then recorded by the airborne sensor. Compared to rural areas, urban and industry areas usually exhibit an enhancement in value of surface reflectance and subsequently an increment of AMF. As shown in Fig. 7, the dependency of the AMF on the surface reflectance is very strong. Also a strong variability of surface reflectance and AMF can be observed in these areas.

210 In this paper we use Landsat 8 surface reflectance product (Vermote et al., 2016) of coastal aerosol band (band 1) as input parameter in AMF calculation. The surface reflectance is retrieved through atmospheric correction, using the Second Simulation of the Satellite Signal in the Solar Spectrum Vectorial (6SV) model (Vermote et al., 1997). Since there is no overpass on the same day inside UVHIS research flight area, we choose surface reflectance product on 3 May 2018 considering the sunny weather condition and no cloud presence. The spatial resolution of Landsat is about 30 m, which is



215 slightly larger than UVHIS. A resampling of Landsat 8 surface reflectance product based on nearest neighbour interpolation is performed for every UVHIS ground pixel.

2. AMF dependence on profiles

Based on airborne UVHIS retrieval product, the horizontal distribution of NO₂ can be detected, but the vertical distribution of NO₂ in the atmosphere is not available. The assumptions we made for profile shape of trace gas and aerosol extinction do
220 not consider the effective variability during research flight, which can be expected in an urban area. Focusing on the impact of different profile shapes on the AMF computation, sensitivity tests of two different NO₂ profiles which are closer to ground surface are performed: well-mixed NO₂ box profile of 0.5 and 1 km height. Compared to the box profile of 2 km which is close to the height of PBL, AMFs decrease by an average of 13 % in the case of a box profile of 1.0 km, while AMFs decrease by an average of 22 % in the case of a box profile of 0.5 km.

225 Depending on the relative position of aerosol and trace gas layer, the optical thickness and scattering properties, aerosols can enhance or reduce the AMF in different ways [28]. If an aerosol layer is located above the majority of the trace gas, the aerosols with high SSA have a shielding effect as less solar scatter light pass through the trace gas layer, leading to a shorter light path. On the other hand, if aerosols and the trace gas are present in the same layer, aerosols can lead to multiple scattering effects which extend the light path and result a larger AMF. According to the simulations of a well-mixed aerosol
230 box profile of 2 km and a pure Rayleigh atmosphere, AMFs are slightly higher (about 1 %) compared to pure Rayleigh scenario.

3. AMF dependence on sun and viewing geometries

As can be seen in Fig. 5, the effect of sun and viewing geometries on AMFs is very small. Based on previous study of Tack et al. (2017), the changing SZA have the greatest effect on AMFs, among other sun and viewing geometries. The SZA varies
235 from 12.8° to 37.4° during the 3 h research flight, and AMF at the end of the flight is 10 % larger than at the beginning of the flight when other parameters are assigned to mean value (Fig. 8). Generally, a larger SZA could result a longer light path through the atmosphere and thus a larger AMF.

4. AMF dependence on the analysis wavelength

The dependence of AMF on analysis wavelength is shown in Fig. 9. It is obvious that the AMF increase with the analysis
240 wavelength. This could be explained by Rayleigh scattering characteristics: photons at shorter wavelengths are more scattered before NO₂ layer than photons at longer wavelengths, leading to the reduced sensitivity to AMF at shorter wavelengths. In the DOAS analysis wavelength window of 430-470 nm, the increase in AMF is about 2 %.



4.4 Geo-referencing and mapping

Accurate geo referencing is essential for emission source locating and data comparison, and can be achieved with sensor
245 position and orientation information recorded by navigation system and IMU on-board. After geo-referencing, the NO₂
VCDs are gridded to combine overlapped adjacent measurements, with a spatial resolution of 0.0003° × 0.0002°.
Corresponding to 27 × 22 m², the grid size used is slightly larger than the effective spatial resolution of the UVHIS for the
purpose of reducing the number of empty grid cells. All VCDs are assigned to a grid cell based on its centre coordinates, and
several VCDs in one grid cell are unweighted averaged. The final NO₂ VCD distribution map is plotted over satellite Maps
250 layers in QGIS 3.8 software (QGIS development team, 2020).

5 Results

The NO₂ VCD two-dimensional distribution map is shown in Fig. 10 for the research flight on 23 June 2018. In general, with
a high performance of UVHIS in spectral and spatial resolution, Figure 10 shows fine-scale NO₂ spatial variability to resolve
individual emission sources. The NO₂ distribution is dominated by several exhaust plumes with enhanced NO₂ concentration
255 compared to other areas, which share a largely consistent transportation pattern from south to north. The largest plume with
peak values of up to 3 × 10¹⁶ molec cm⁻², is transporting for at least 9 km downwind inside the observation area. The map is
built from 13 overlapped adjacent flight lines, the acquisition time of every track is about 10 minutes. Due to temporal
discontinuity of flight lines and dynamic characteristics of NO₂ field, biases can be observed between adjacent flight lines,
especially inside the polluted area when wind direction is changed.

260 Inside flight area, the predominant NO₂ sources are mainly related to anthropogenic emitters in the northwest part. These
sources include a power plant, a steel factory, two cement factories, several carbon factories etc. A strong gradient from
south to north is shown in all plumes, consistent with the southerly wind direction. The largest plume originates from an
emitter inside a steel factory, which is represented by number 3 in Fig. 10. This dominant plume is transporting at least 9 km
from south to north and seems to be continuing outside the flight region. As the plume spreads further north, it becomes
265 much broader. However, it is discontinuous and inhomogeneous in the distribution map, because of time differences among
adjacent flight lines, as well as a dynamically changing NO₂ field which is related to wind direction and speed. As shown in
Fig. 10, this plume reaches its peak value outside the steel factory, at a small valley about 1 km to the north. This enhanced
level of NO₂ may be caused by terrain factor which contributes to the accumulation of pollution gases.

Number 4 in Fig. 10 represents an isolated exhaust plume originated from another emitter inside the steel factory, with a
270 peak value of 1.4 × 10¹⁶ molec cm⁻². A weaker plume with peak values of 1.0 × 10¹⁶ molec cm⁻² is also detected by UVHIS,
which seems to originate from the power plant. Indicated by number 2 in Fig. 10, this power plant is less than 2 km south of
the steel factory. Number 1 in Fig. 10 indicates several carbon factories, which are located on the left side of the flight area.
Several plumes with peak values of 1.5 × 10¹⁶ molec cm⁻², gradually merge together during the transportation downwind.



Number 5 and Number 6 in Fig. 10 represent two different cement factories. Peak values of these two plumes are 1.5×10^{16} molec cm^{-2} and 1.3×10^{16} molec cm^{-2} respectively.

The urban areas of Feicheng city and Pingyin county are located on the right side, and on the upper left corner of the flight area respectively. Compared to the industrial areas mentioned above, the pollution levels of the rural and urban areas are much lower due to the lack of contributing sources, ranging from 1 to 4×10^{15} molec cm^{-2} .

6 Discussion

6.1 Uncertainty analysis

The total uncertainty on the retrieved NO_2 VCDs is composed of three parts: (1) uncertainties in the retrieved dSCDs; (2) uncertainties in reference column SCD_{ref} ; (3) uncertainties in computed AMFs. Assuming that these uncertainties originating from independent steps are sufficiently uncorrelated, the total uncertainty of NO_2 VCD can be quantified as follows:

$$\sigma_{\text{VCD}_i} = \sqrt{\left(\frac{\sigma_{\text{dSCD}_i}}{\text{AMF}_i}\right)^2 + \left(\frac{\sigma_{\text{SCD}_{\text{ref}}}}{\text{AMF}_i}\right)^2 + \left(\frac{\text{SCD}_i}{\text{AMF}_i^2} \times \sigma_{\text{AMF}_i}\right)^2} \quad (2)$$

The first uncertainty source, σ_{dSCD_i} , originates from DOAS fit residuals and is a direct output in QDOAS software. This dSCD uncertainty is dominated by shot noise from radiance, electronic noise from the instrument, uncertainties from the cross sections and errors from wavelength calibration. In this study, spatial binning of 10 pixels is performed to reduce this DOAS fit residuals, with a mean slant error of 4.8×10^{15} molec cm^{-2} . Compared to mobile DOAS system, this DOAS fit error is approximately two times larger. Unlikely situation of mobile DOAS system, it becomes a major contributor to the total uncertainty in the case of an airborne sensor, especially in a clean area.

The second uncertainty source, $\sigma_{\text{SCD}_{\text{ref}}}$, is caused by the NO_2 residual amount in the reference spectra. Since no direct measurement of the NO_2 column is performed in the reference area, an uncertainty of 100 % is assumed on the estimated NO_2 background amount. This results in an uncertainty of 1.0×10^{15} molec cm^{-2} in the background column.

The third uncertainty source, σ_{AMF_i} , derives from uncertainties in the parameter assumptions of radiative transfer model inputs. According to previous studies (Boersma et al., 2004; Pope et al., 2015), it is treated as systematic and depends on the surface albedo, NO_2 profile, aerosol parameters, and cloud fraction. (1) Since the research flight took place under cloudless conditions, cloud fraction is neglected in this case. (2) Results of the dependence tests in Sect. 4.3.2 suggest that the surface albedo has the most significant effect on the AMF. According to Vermote et al. (2016), the uncertainty of LANDSAT 8 surface reflectance product of band 1 is 0.011. (3) Based on the sensitivity study performed in Sect. 4.3.2, the uncertainty related to the a priori NO_2 profile shape is lower than 22 %. (4) According to the performed simulations of a pure Rayleigh atmosphere, the uncertainty related to aerosol state is estimated to be less than 1 %. (5) Because of the high accuracy of the



viewing and sun geometry, and its low impact on the AMF computation revealed in the previous section, the uncertainty related to viewing and sun geometry is expected to be ignorable. Therefore, combining all uncertainty sources in quadrature, a mean relative uncertainty of 24 % on the σ_{AMF_i} is obtained.

305 Based on above discussion, the total uncertainties on the retrieved NO_2 VCDs of all observations of the research flight are calculated. They typically range between 1 and 5×10^{15} molec cm^{-2} , with a mean value of 2.6×10^{15} molec cm^{-2} .

6.2 Comparison to mobile DOAS measurements

In order to compare UVHIS NO_2 VCDs to ground-based measurements, mobile DOAS observations were performed on 23 June 2018 as well. This mobile DOAS system is composed of a spectrum acquisition unit and a GPS module. The spectrum
310 collection unit consists of a spectrometer, a telescope, an optical fiber, and a workbench. The FOV of this telescope is 0.3° , and its focal length is 69 mm. The spectrometer used is a Maya 2000 Pro spectrometer, with a wavelength range of 260–420 nm and a spectral resolution of 0.55 nm. Zenith-sky observations of mobile DOAS are adopted for minimal blocking of buildings and trees in this research. The important properties of the mobile DOAS system and its NO_2 retrieval approach are shown in Table 5.

315 Basically, the route of the mobile DOAS is designed to encircle the power plant and steel factory which are supposed to be predominant sources. For the comparison, mobile DOAS observations are first gridded to the same sampling of UVHIS pixels, then the VCD of UVHIS NO_2 results is extracted for each co-located mobile measurement. An overview of the mobile DOAS measurements over UVHIS NO_2 layer is shown in Fig. 11. It is obvious that NO_2 distributions of mobile DOAS system and UVHIS exhibit similar spatial characteristics, which low values are located in the south of the steel
320 factory and power plant, and high values are near the downwind of several plumes.

Figure 12 shows scatter plots with VCDs retrieved by UVHIS on the x-axis and mobile DOAS VCDs on the y-axis. The corresponding results of linear regression analysis are also provided in Fig. 12, with a correlation coefficient of 0.65, a slope of 1.04, and an intercept of 3.27×10^{13} . In general, an overestimation of mobile DOAS VCDs of increased value can be observed. The absolute time offset between mobile DOAS and airborne observations can be up to 1 h, which means that both
325 instruments cannot sample the NO_2 column at certain geolocation simultaneously. Considering the variability in local emissions and meteorology, it is reasonable that the differences between these two instruments exist. Besides, the averaging effect of the area inside an UVHIS pixel can also lead to the underestimation of UVHIS compared to mobile DOAS system.

7 Conclusions

In this paper, we present the newly developed Ultraviolet Visible Hyperspectral Imaging Spectrometer (UVHIS), with a
330 broad spectral region from 200 to 500 nm, and a high spectral resolution better than 0.5 nm. The instrument is operated in three channels at wavelength 200 to 276 nm (channel 1), 276 to 380 nm (channel 2), and 380 to 500 nm (channel 3) for



minimal stray light effects and highest spectral performance. The optical design of each channel consists of a fore-optics with a FOV of 40°, an Offner imaging spectrometer, and a CCD array detector of 1032 × 1072 pixels.

335 Also we present the first NO₂ retrieval results from the UVHIS airborne observation in June 2018. The research flight above Feicheng, China, covered an area of about 20 × 30 km² within 3 h, with a high spatial resolution about 25 × 22 m². We first retrieve the differential NO₂ slant column densities from nadir observed spectra by application of DOAS technique, to a mean reference spectra over a clean area. Then we convert those NO₂ slant columns to vertical columns using air mass factors derived from SCIATRAN model with Landsat 8 surface reflectance product. Total uncertainties of NO₂ vertical columns are in range of 1 to 5 × 10¹⁵ molec cm⁻², with a mean value of 2.6 × 10¹⁵ molec cm⁻².

340 The two-dimensional distribution map of NO₂ VCD demonstrates that UVHIS is adequate for trace gas pollution monitoring over a large area in a relative short time frame. With the high spatial resolution of UVHIS, different local emission sources can be distinguished, fine-scale horizontal variability can be revealed, and trace gas emission and transmission can be understood. For the flight on 23 June 2018, NO₂ distribution is dominated by several exhaust plumes which exhibit same south to north direction of transmission, with a peak value of 3 × 10¹⁶ molec cm⁻² in the dominant plume. Comparisons of
345 UVHIS NO₂ vertical columns to mobile DOAS observations show good agreement overall, with a correlation coefficient of 0.65 for all co-located measurements. However, an underestimation of the high NO₂ columns of UVHIS is observed relative to the mobile DOAS measurements.

High-resolution information about the NO₂ horizontal distribution, generated from UVHIS airborne data, is unique and valuable compared to ground-based instruments and space-borne sensors. In future study, UVHIS could be applied in
350 validation of satellite trace gas instruments, and in connection between local point observations, air quality models, and global monitoring from space.

Author Contributions: Conceptualization, F.S.; methodology, Y.J. and H.Z.; software, Z.C.; validation, X.Q. and D.Y.; formal analysis, L.X.; resources, K.Z.; writing—original draft preparation, L.X.; writing—review and editing, F.S.

355

Acknowledgments: We would like to thank Thomas Danckaert, Caroline Fayt and Michel Van Roozendaal for help on QDOAS software.

Conflicts of Interest: The authors declare no conflict of interest.

360



References

- Barsi, J., Schott, J., Hook, S., Raqueno, N., Markham, B. and Radocinski, R.: Landsat-8 Thermal Infrared Sensor (TIRS) Vicarious Radiometric Calibration, *Remote Sens.*, 6(11), 11607–11626, doi:10.3390/rs61111607, 2014.
- 365 Boersma, K. F., Eskes, H. J. and Brinksma, E. J.: Error analysis for tropospheric NO₂ retrieval from space: ERROR ANALYSIS FOR TROPOSPHERIC NO₂, *J. Geophys. Res. Atmospheres*, 109(D4), n/a-n/a, doi:10.1029/2003JD003962, 2004.
- Bovensmann, H., Burrows, J. P., Buchwitz, M. and Frerick, J.: SCIAMACHY: Mission Objectives and Measurement Modes, *J. ATMOSPHERIC Sci.*, 56, 24, 1999.
- 370 Burrows, J. P., Weber, M., Buchwitz, M., Rozanov, V., TTER-WEIßENMAYER, A. L., Richter, A., Bramstedt, K., Eichmann, K.-U., Eisinger, M. and Perner, D.: The Global Ozone Monitoring Experiment (GOME): Mission Concept and First Scientific Results, *J. ATMOSPHERIC Sci.*, 56, 25, 1999.
- Chance, K. and Kurucz, R. L.: An improved high-resolution solar reference spectrum for earth's atmosphere measurements in the ultraviolet, visible, and near infrared, *J. Quant. Spectrosc. Radiat. Transf.*, 111(9), 1289–1295, doi:10.1016/j.jqsrt.2010.01.036, 2010.
- 375 Chance, K. V. and Spurr, R. J. D.: Ring effect studies: Rayleigh scattering, including molecular parameters for rotational Raman scattering, and the Fraunhofer spectrum, *Appl. Opt.*, 36(21), 5224, doi:10.1364/AO.36.005224, 1997.
- Cheng, L., Tao, J., Valks, P., Yu, C., Liu, S., Wang, Y., Xiong, X., Wang, Z. and Chen, L.: NO₂ Retrieval from the Environmental Trace Gases Monitoring Instrument (EMI): Preliminary Results and Intercomparison with OMI and TROPOMI, *Remote Sens.*, 11(24), 3017, doi:10.3390/rs11243017, 2019.
- 380 Danckaert, T., Fayt, C., Roozendael, M. V., Smedt, I. D., Letocart, V., Merlaud, A. and Pinardi, G.: QDOAS Software user manual, [online] Available from: http://uv-vis.aeronomie.be/software/QDOAS/QDOAS_manual.pdf (Accessed 2 June 2020), 2020.
- Heue, K.-P., Wagner, T., Broccardo, S. P., Walter, D., Piketh, S. J., Ross, K. E., Beirle, S. and Platt, U.: Direct observation of two dimensional trace gas distributions with an airborne Imaging DOAS instrument, *Atmospheric Chem. Phys.*, 8(22), 6707–6717, doi:10.5194/acp-8-6707-2008, 2008.
- 385 Lawrence, J. P., Anand, J. S., Vande Hey, J. D., White, J., Leigh, R. R., Monks, P. S. and Leigh, R. J.: High-resolution measurements from the airborne Atmospheric Nitrogen Dioxide Imager (ANDI), *Atmospheric Meas. Tech.*, 8(11), 4735–4754, doi:10.5194/amt-8-4735-2015, 2015.
- 390 Levelt, P. F., van den Oord, G. H. J., Dobber, M. R., Malkki, A., Huib Visser, Johan de Vries, Stammes, P., Lundell, J. O. V. and Saari, H.: The ozone monitoring instrument, *IEEE Trans. Geosci. Remote Sens.*, 44(5), 1093–1101, doi:10.1109/TGRS.2006.872333, 2006.
- Liu, J., Si, F., Zhou, H., Zhao, M., Dou, K., Wang, Y. and Liu, W.: Observation of two-dimensional distributions of NO₂ with airborne imaging DOAS technology, *Acta Phys. Sin.*, 64(3), 034217, doi:10.7498/aps.64.034217, 2015.
- 395 Meier, A. C., Schönhardt, A., Bösch, T., Richter, A., Seyler, A., Ruhtz, T., Constantin, D.-E., Shaiganfar, R., Wagner, T., Merlaud, A., Van Roozendael, M., Belegante, L., Nicolae, D., Georgescu, L. and Burrows, J. P.: High-resolution airborne imaging DOAS measurements of NO₂ above Bucharest during AROMAT, *Atmospheric Meas. Tech.*, 10(5), 1831–1857, doi:10.5194/amt-10-1831-2017, 2017.



- 400 Munro, R., Lang, R., Klaes, D., Poli, G., Retscher, C., Lindstrot, R., Huckle, R., Lacan, A., Grzegorski, M., Holdak, A., Kokhanovsky, A., Livschitz, J. and Eisinger, M.: The GOME-2 instrument on the Metop series of satellites: instrument design, calibration, and level 1 data processing – an overview, *Atmospheric Meas. Tech.*, 9(3), 1279–1301, doi:10.5194/amt-9-1279-2016, 2016.
- Platt, U. and Stutz, J.: *Differential Optical Absorption Spectroscopy: Principles and Applications*, Springer-Verlag, Berlin, Germany., 2008.
- 405 Pope, R. J., Chipperfield, M. P., Savage, N. H., Ordóñez, C., Neal, L. S., Lee, L. A., Dhomse, S. S., Richards, N. A. D. and Keslake, T. D.: Evaluation of a regional air quality model using satellite column NO₂: treatment of observation errors and model boundary conditions and emissions, *Atmospheric Chem. Phys.*, 15(10), 5611–5626, doi:10.5194/acp-15-5611-2015, 2015.
- 410 Popp, C., Brunner, D., Damm, A., Van Roozendael, M., Fayt, C. and Buchmann, B.: High-resolution NO₂ remote sensing from the Airborne Prism Experiment (APEX) imaging spectrometer, *Atmospheric Meas. Tech.*, 5(9), 2211–2225, doi:10.5194/amt-5-2211-2012, 2012.
- QGIS development team: QGIS Geographic Information System, Open Source Geospatial Foundation, QGIS Geogr. Inf. Syst. Open Source Geospatial Found. [online] Available from: <https://www.qgis.org/en/site/> (Accessed 2 June 2020), 2020.
- 415 Remer, L. A., Kaufman, Y. J., Tanré, D., Mattoo, S., Chu, D. A., Martins, J. V., Li, R.-R., Ichoku, C., Levy, R. C., Kleidman, R. G., Eck, T. F., Vermote, E. and Holben, B. N.: The MODIS Aerosol Algorithm, Products, and Validation, *J. Atmospheric Sci.*, 62(4), 947–973, doi:10.1175/JAS3385.1, 2005.
- Rozanov, V. V., Rozanov, A. V., Kokhanovsky, A. A. and Burrows, J. P.: Radiative transfer through terrestrial atmosphere and ocean: Software package SCIATRAN, *J. Quant. Spectrosc. Radiat. Transf.*, 133, 13–71, doi:10.1016/j.jqsrt.2013.07.004, 2014.
- 420 Seinfeld, J. H. and Pandis, S. N.: *Atmospheric chemistry and physics: from air pollution to climate change*, Third edition., John Wiley & Sons, Hoboken, New Jersey., 2016.
- Serdyuchenko, A., Gorshchev, V., Weber, M., Chehade, W. and Burrows, J. P.: High spectral resolution ozone absorption cross-sections – Part 2: Temperature dependence, *Atmospheric Meas. Tech.*, 7(2), 625–636, doi:10.5194/amt-7-625-2014, 2014.
- 425 Solomon, S.: Stratospheric ozone depletion: A review of concepts and history, *Rev. Geophys.*, 37(3), 275–316, doi:10.1029/1999RG900008, 1999.
- Solomon, S., Schmeltekopf, A. L. and Sanders, R. W.: On the interpretation of zenith sky absorption measurements, *J. Geophys. Res.*, 92(D7), 8311, doi:10.1029/JD092iD07p08311, 1987.
- 430 Tack, F., Merlaud, A., Iordache, M.-D., Danckaert, T., Yu, H., Fayt, C., Meuleman, K., Deutsch, F., Fierens, F. and Van Roozendael, M.: High-resolution mapping of the NO₂ spatial distribution over Belgian urban areas based on airborne APEX remote sensing, *Atmospheric Meas. Tech.*, 10(5), 1665–1688, doi:10.5194/amt-10-1665-2017, 2017.
- 435 Tack, F., Merlaud, A., Meier, A. C., Vlemmix, T., Ruhtz, T., Iordache, M.-D., Ge, X., van der Wal, L., Schuettmeyer, D., Ardelean, M., Calcan, A., Constantin, D., Schönhardt, A., Meuleman, K., Richter, A. and Van Roozendael, M.: Intercomparison of four airborne imaging DOAS systems for tropospheric NO₂ mapping – the AROMAPEX campaign, *Atmospheric Meas. Tech.*, 12(1), 211–236, doi:10.5194/amt-12-211-2019, 2019.



- Thalman, R. and Volkamer, R.: Temperature dependent absorption cross-sections of O₂–O₂ collision pairs between 340 and 630 nm and at atmospherically relevant pressure, *Phys. Chem. Chem. Phys.*, 15(37), 15371, doi:10.1039/c3cp50968k, 2013.
- 440 Vandaele, A. C., Hermans, C., Simon, P. C., Carleer, M., Colin, R., Fally, S., Mérienne, M. F., Jenouvrier, A. and Coquart, B.: Measurements of the NO₂ absorption cross-section from 42 000 cm⁻¹ to 10 000 cm⁻¹ (238–1000 nm) at 220 K and 294 K, *J. Quant. Spectrosc. Radiat. Transf.*, 59(3–5), 171–184, doi:10.1016/S0022-4073(97)00168-4, 1998.
- 445 Veefkind, J. P., Aben, I., McMullan, K., Förster, H., de Vries, J., Otter, G., Claas, J., Eskes, H. J., de Haan, J. F., Kleipool, Q., van Weele, M., Hasekamp, O., Hoogeveen, R., Landgraf, J., Snel, R., Tol, P., Ingmann, P., Voors, R., Kruizinga, B., Vink, R., Visser, H. and Levelt, P. F.: TROPOMI on the ESA Sentinel-5 Precursor: A GMES mission for global observations of the atmospheric composition for climate, air quality and ozone layer applications, *Remote Sens. Environ.*, 120, 70–83, doi:10.1016/j.rse.2011.09.027, 2012.
- Vermote, E., Justice, C., Claverie, M. and Franch, B.: Preliminary analysis of the performance of the Landsat 8/OLI land surface reflectance product, *Remote Sens. Environ.*, 11, 2016.
- 450 Vermote, E. F., Tanre, D., Deuze, J. L., Herman, M. and Morcette, J.-J.: Second Simulation of the Satellite Signal in the Solar Spectrum, 6S: an overview, *IEEE Trans. Geosci. Remote Sens.*, 35(3), 675–686, doi:10.1109/36.581987, 1997.
- Zhang, Q., Huang, S., Zhao, X., Si, F., Zhou, H., Wang, Y. and Liu, W.: The Design and Implementation of CCD Refrigeration System of Imaging Spectrometer, *Acta Photonica Sin.*, 46(3), 0311004, 2017.
- 455 Zhao, M. J., Si, F. Q., Zhou, H. J., Wang, S. M., Jiang, Y. and Liu, W. Q.: Preflight calibration of the Chinese Environmental Trace Gases Monitoring Instrument (EMI), *Atmospheric Meas. Tech.*, 11(9), 5403–5419, doi:10.5194/amt-11-5403-2018, 2018.

460

465

470



Table 1: UVHIS instrument characteristics of three channels.

Characteristic	Channel 1	Channel 2	Channel 3
Wavelength range	200-276 nm	276-380 nm	380-500 nm
Spectral sampling	0.074 nm	0.10 nm	0.12 nm
Spectral resolution	0.34 nm	0.46 nm	0.49 nm
FOV	40°	40°	40°
Focal length	18 mm	18 mm	18 mm
Across-track angular resolution	0.5 mrad	0.5 mrad	0.5 mrad
f-number	3.4	3.6	3.6
Detector size	1032 × 1072	1032 × 1072	1032 × 1072

475

Table 2. Preflight wavelength calibration results of UVHIS channel 3.

FOV	379.887 nm	404.656 nm	450.504 nm	500.566 nm
-20°	0.35 nm	0.35 nm	0.39 nm	0.50 nm
-15°	0.33 nm	0.31 nm	0.33 nm	0.43 nm
-10°	0.31 nm	0.29 nm	0.29 nm	0.41 nm
-5°	0.31 nm	0.30 nm	0.29 nm	0.34 nm
0°	0.31 nm	0.32 nm	0.30 nm	0.30 nm
5°	0.34 nm	0.36 nm	0.34 nm	0.30 nm
10°	0.38 nm	0.39 nm	0.38 nm	0.32 nm
15°	0.40 nm	0.44 nm	0.42 nm	0.35 nm
20°	0.45 nm	0.46 nm	0.47 nm	0.38 nm

480

485



Table 3. Main analysis parameters and absorption cross sections for NO₂ DOAS retrieval.

Parameter	Settings
Wavelength calibration	Solar atlas, (Chance and Kurucz, 2010)
Fitting interval	430-470 nm
Cross sections	
NO ₂	298 K, Vandaele et al. (1998)
O ₃	223 K, Serdyuchenko et al. (2014)
O ₄	293 K, Thalman and Volkamer (2013)
Ring effect	Chance and Spurr (1997)
Polynomial term	Order 5
Intensity offset	Order 1

490

495

Table 4. Overview of the input parameters in the SCIATRAN RTM, characterizing the AMF LUT.

RTM Parameter	Grid settings
Wavelength	450 nm
Sensor altitude	3 km
Surface reflectance	0.01-0.4 (steps of 0.01)
Solar zenith angle	10-40° (steps of 10°)
Viewing zenith angle	0-40° (steps of 10°)
Relative azimuth angle	0-180° (steps of 30°)
Aerosol optical depth	0-1 (steps of 0.1)
Aerosol extinction profile	Box of 2.0 km
NO ₂ profile	Box of 2.0 km

500



Table 5. Properties of the mobile DOAS system and its NO₂ fit.

Parameter	Settings
Elevation angle	zenith
Fitting interval	356-376 nm
Wavelength calibration	Mercury lamp
Cross sections	
NO ₂	298 K, Vandaele et al. (1998)
O ₃	223 K, Serdyuchenko et al. (2014)
O ₄	293 K, Thalman and Volkamer (2013)
Ring effect	Chance and Spurr (1997)
Polynomial term	Order 5
Intensity offset	Order 1

505

510

515

520

525

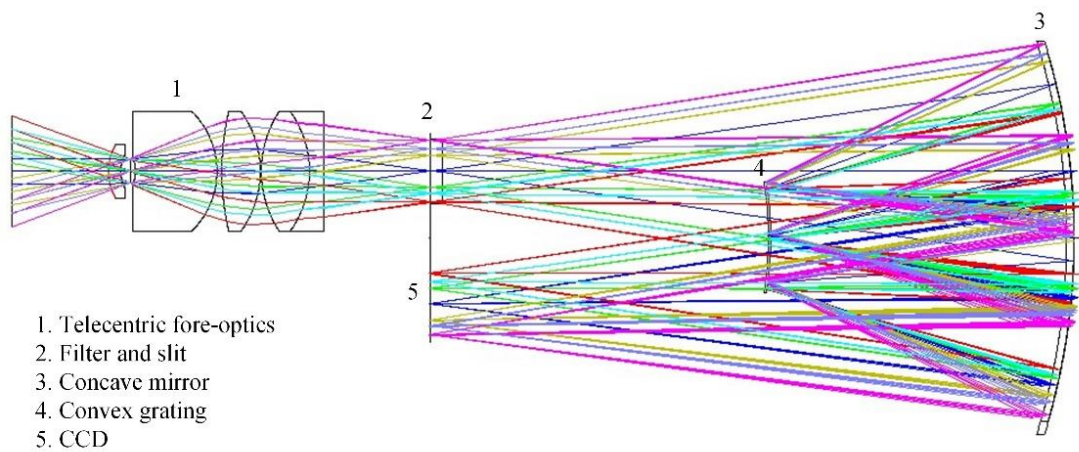


Figure 1. Optical layout of the UVHIS channel 3. Optical design of channel 1 and channel 2 is similar.

530

535

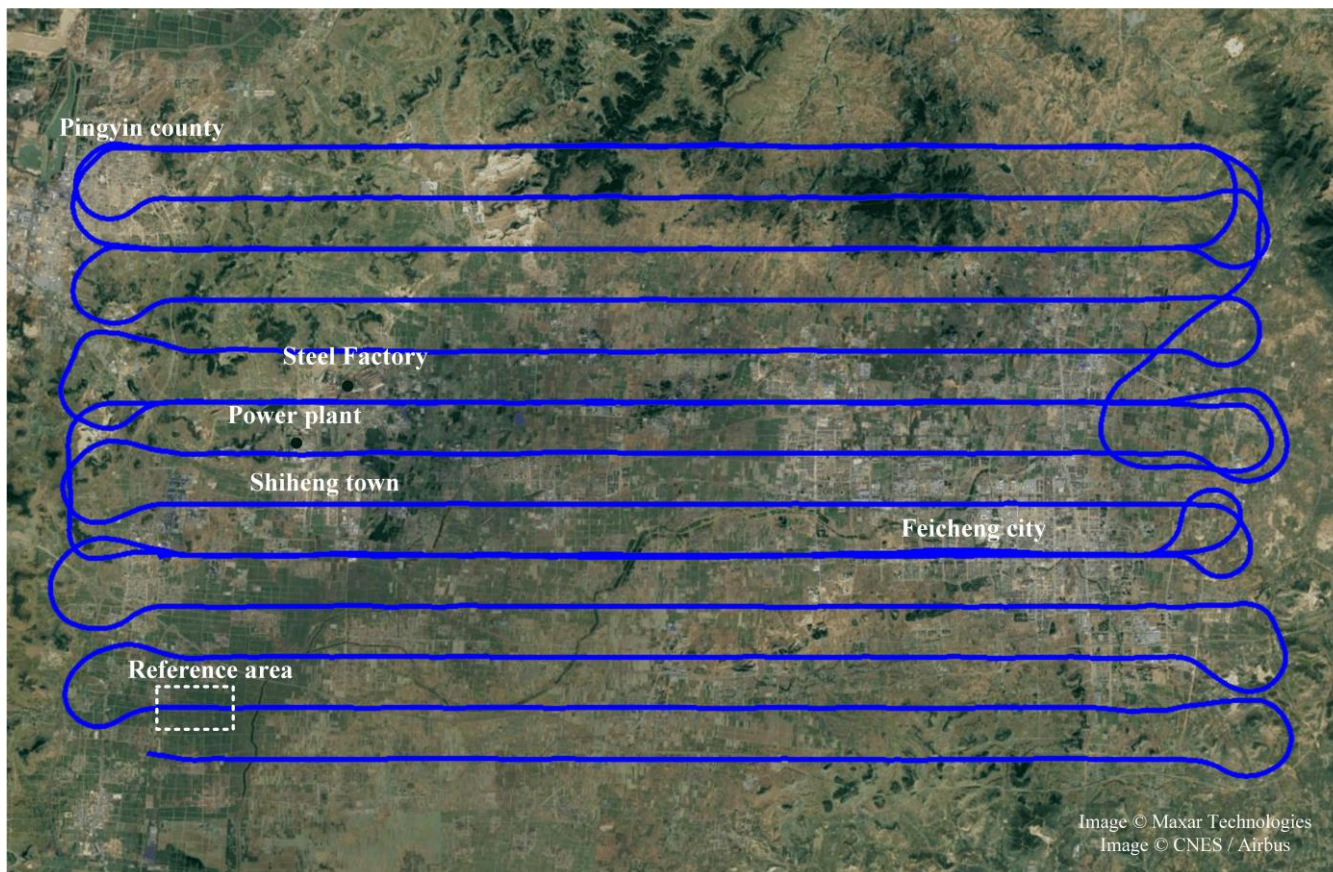


Figure 2. Overview of the demonstration flight. Flight lines are shown in blue. Black dots represent the major emission sources: a steel factory and a power plant. White dashed box represents the reference area.

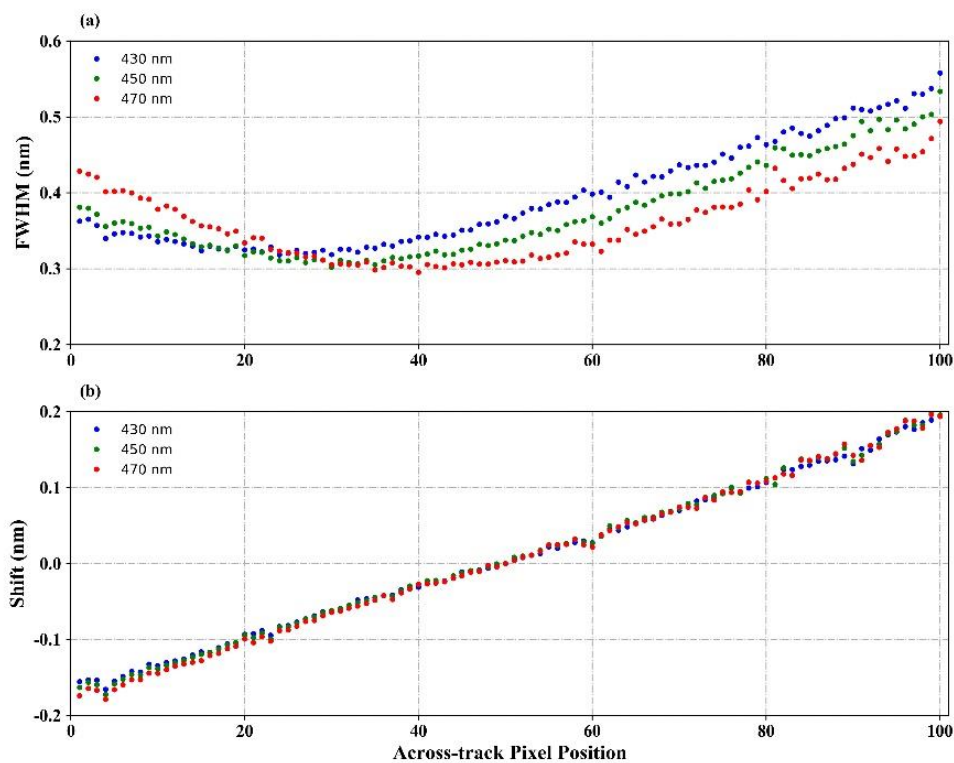


Figure 3. In-flight spectral calibration: (a) the spectral resolution (FWHM); (b) the spectral shift on different across-track position. Results at three wavelengths are plotted: blue for 430 nm, green for 450 nm and red for 470 nm.

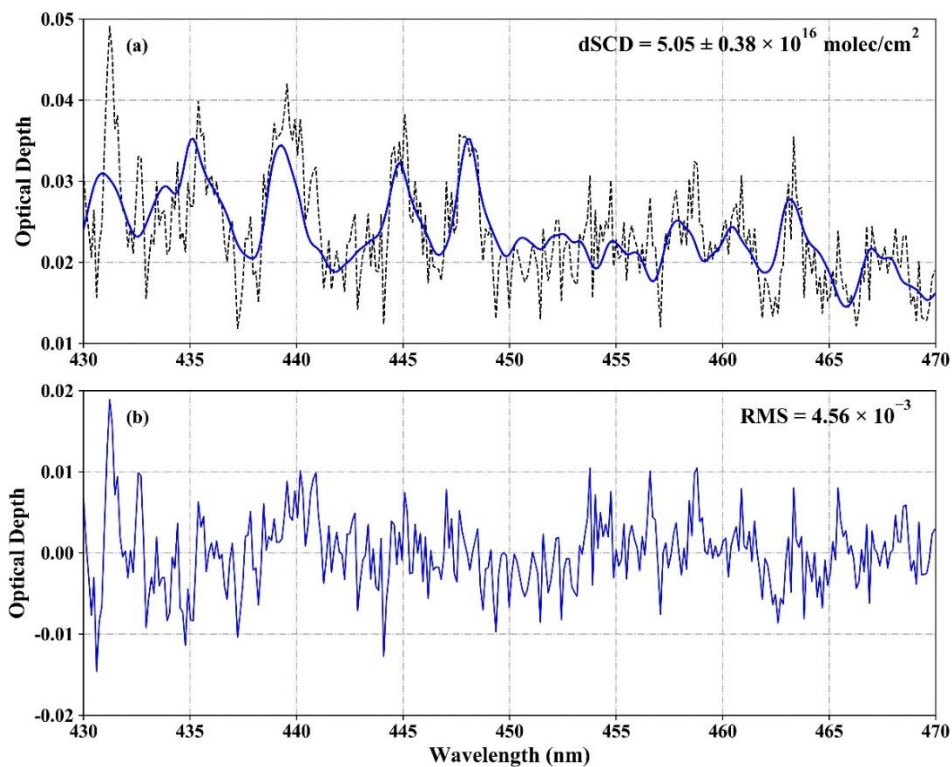


Figure 4. Sample DOAS fit result for NO_2 : (a) observed (black dashed line) and fitted (blue line) optical depths from measured spectra; (b) the remaining residuals of DOAS fit.

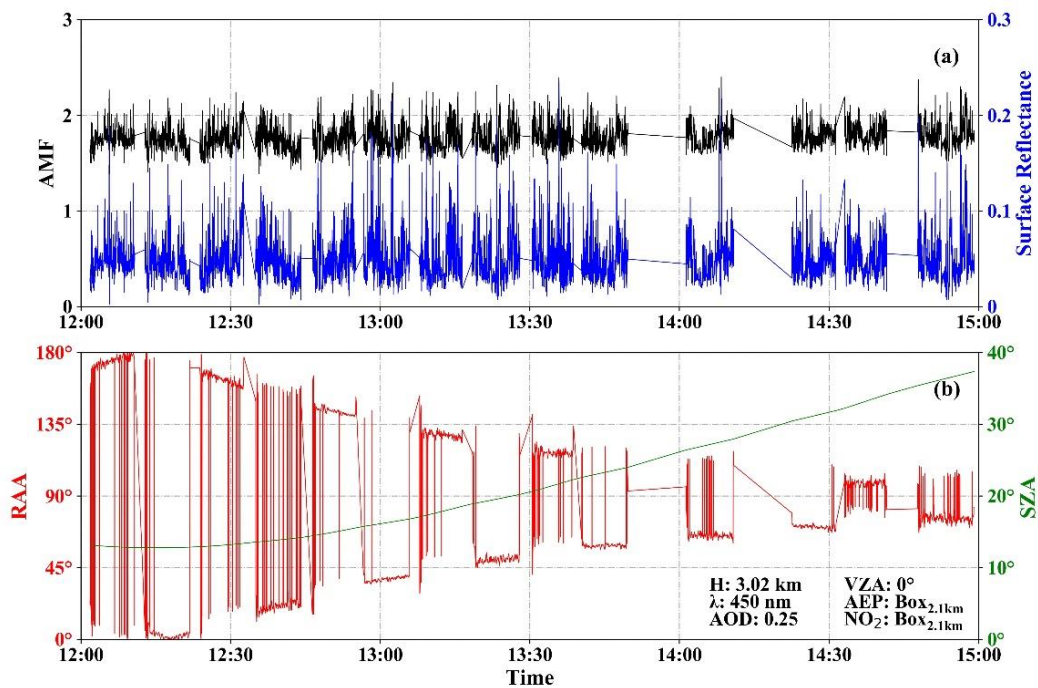


Figure 5. Time series of NO₂ AMF compared with (a) surface reflectance; (b) SZA and RAA for the research flight on 23 June 2018, computed with SCIATRAN model based on the RTM parameters from the UVHIS instrument. Only data of the nadir observations in each flight line are plotted.

555

560

565

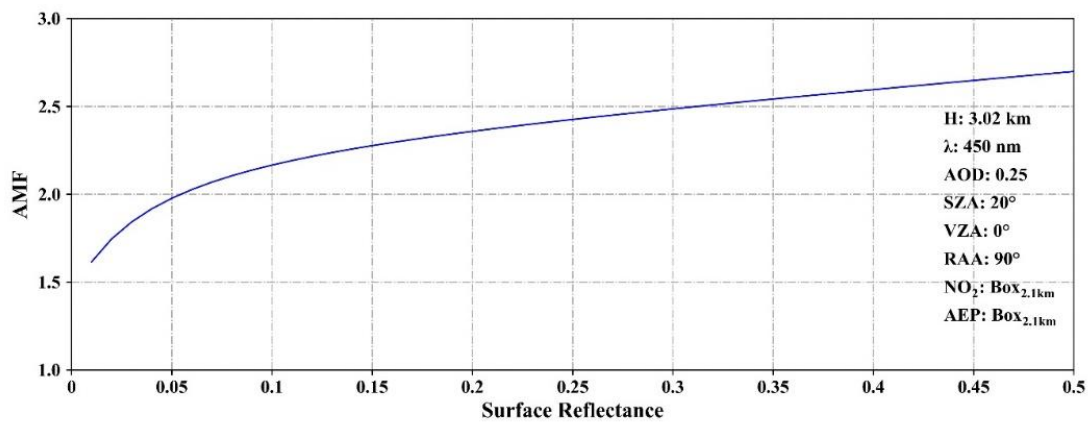


Figure 6. Dependence of the AMF on the surface reflectance. Other parameters are also provided in the figure.

570

575

580

585

590

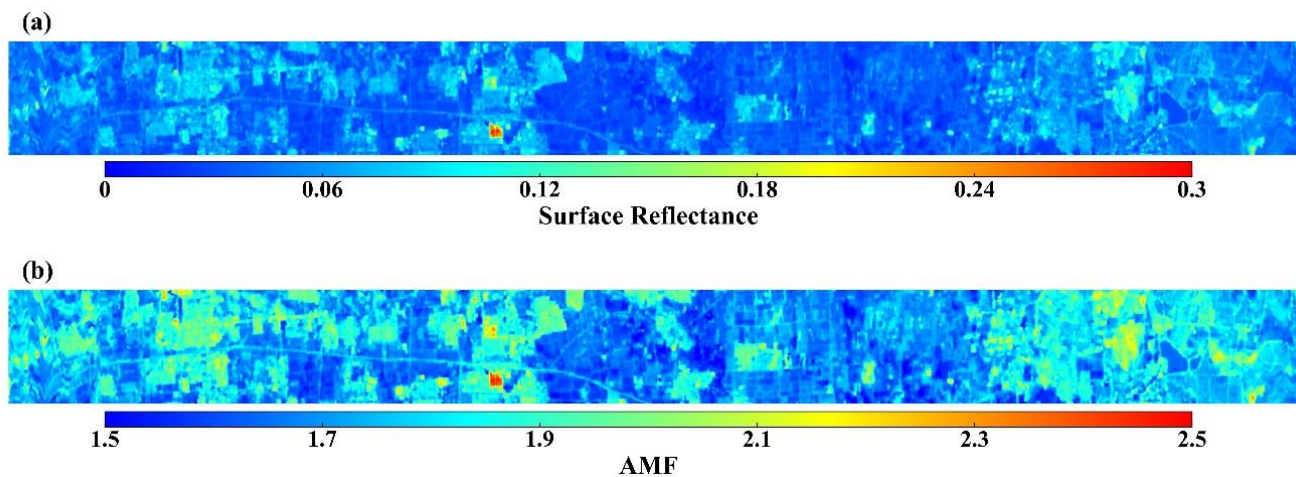


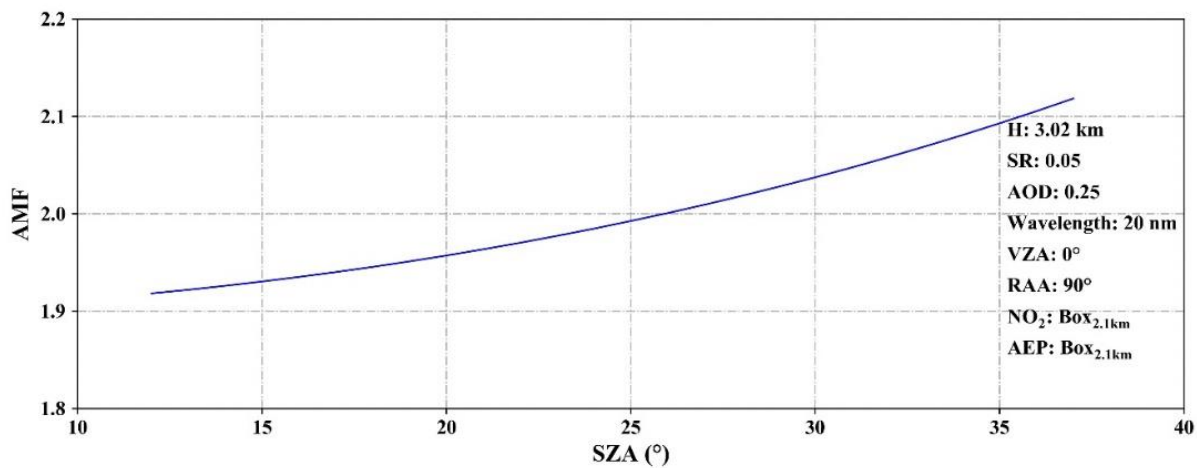
Figure 7. (a) Surface reflectance; (b) computed AMFs, for one flight line of the Feicheng data set. A strong dependency of the AMF on the surface reflectance can be observed.

595

600

605

610



615 **Figure 8.** Dependence of the AMF on the SZA. Other parameters are also provided in the figure.

620

625

630

635

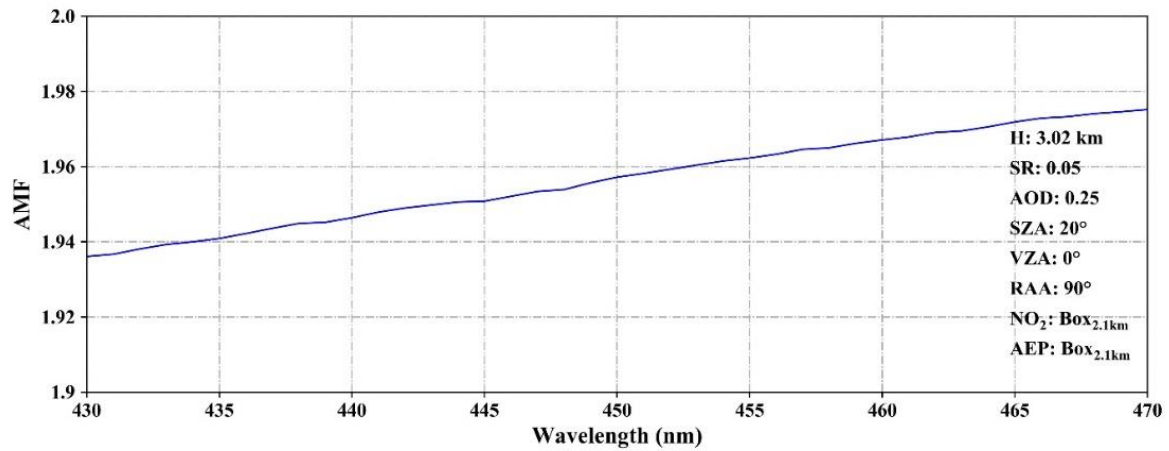


Figure 9. Dependence of the AMF on the analysis wavelength. Other parameters are also provided in the figure.

640

645

650

655

660

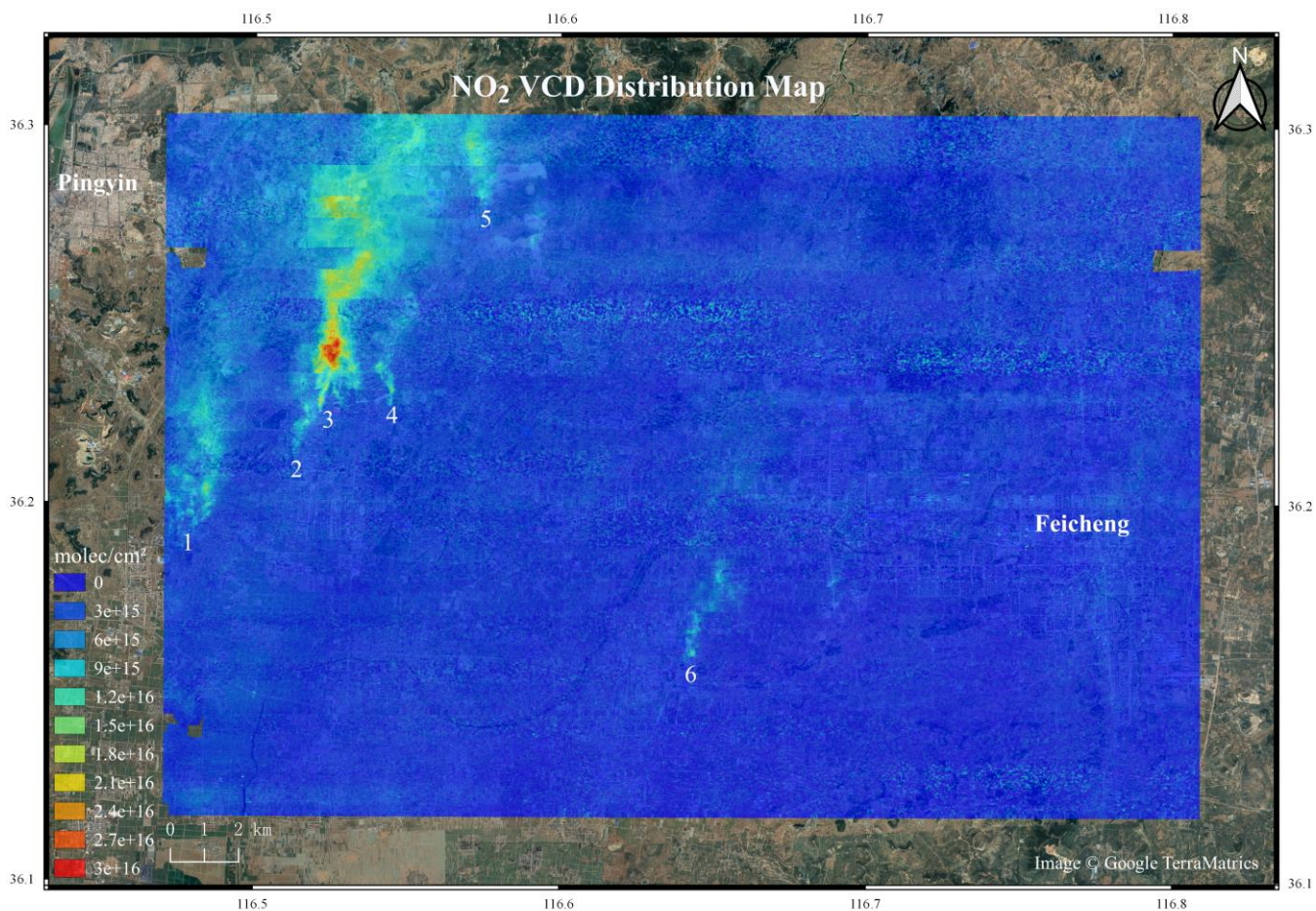


Figure 10. Tropospheric NO₂ VCD map retrieved from UVHIS over Feicheng on 23 June 2018. The major contributing NO₂ emission sources are indicated by number 1 to 6.

665

670

675

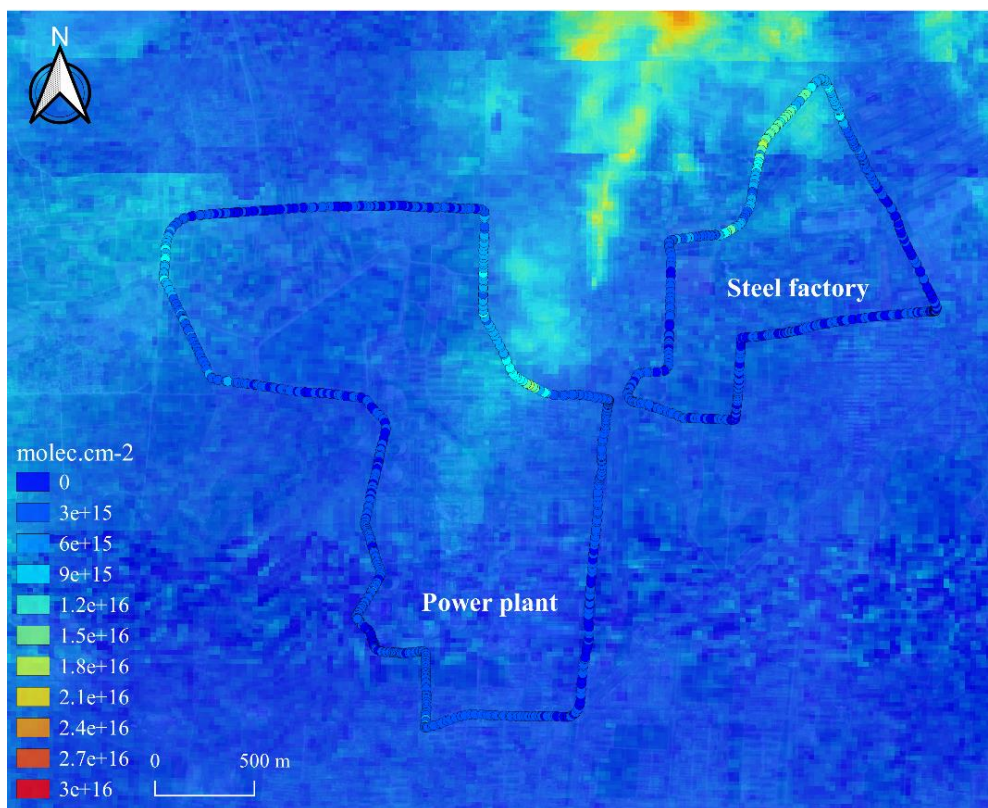
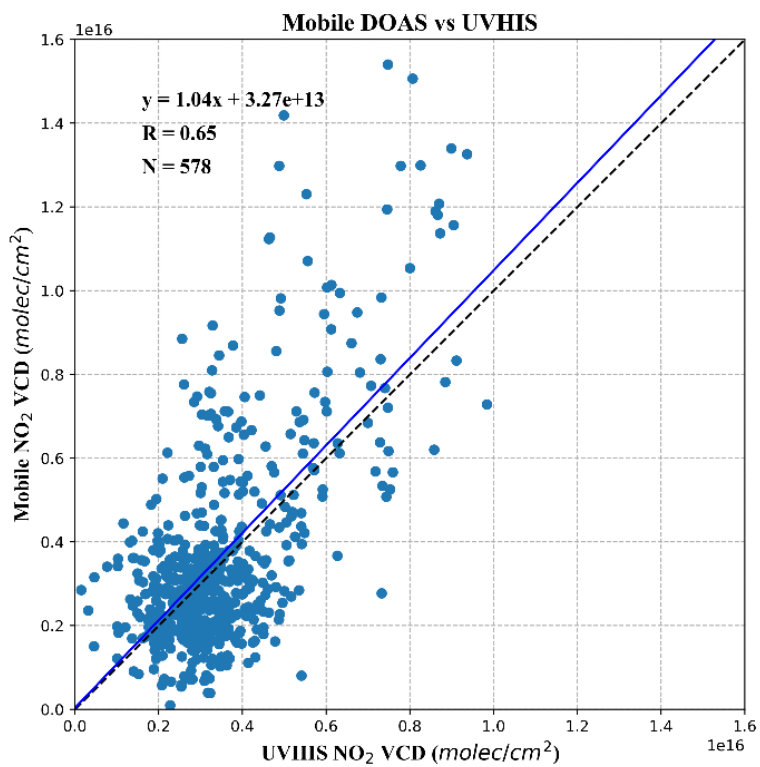


Figure 11. Overview of VCDs retrieved from ground-based mobile DOAS system (circle marks), and VCDs retrieved by UVHIS (background layer), measured on 23 June 2018.

680

685

690



695 **Figure 12.** Scatter plot and linear regression analysis of the co-located NO₂ VCDs, retrieved from UVHIS and mobile DOAS system.

700